Available online at www.sciencedirect.com
SCIENCE DIRECT®
Journal of Nuclear Materials 321 (2003) 281–287
journal of nuclear materials
www.elsevier.com/locate/jnucmat

Nuclear reaction analysis of helium migration in zirconia

J.-M. Costantini [a,*], J.-J. Grob [b], J. Haussy [c], P. Trocellier [d], Ph. Trouslard [e]

[a] CEA-SACLAY, DMN/SRMA, F-91191 Gif-Sur-Yvette cedex, France
[b] PHASE Laboratory/CNRS, 23, Rue du Loess, BP 20, F-67037, Strasbourg cedex, France
[c] CEA-DIF, DCRE/SEIM, BP 12, F-91680 Bruyères-le-Châtel, France
[d] CEA-SACLAY, DMN/SRMP, F-91191 Gif-Sur-Yvette cedex, France
[e] CEA-SACLAY, INSTN, F-91191 Gif-Sur-Yvette cedex, France

Received 10 February 2003; accepted 26 May 2003

Abstract

We have studied helium migration in monoclinic (α-ZrO_2) and cubic yttria-stabilized zirconia, YSZ (ZrO_2:Y) from non-destructive ^{3}He depth profiling using the resonant ^{3}He(d, p)^{4}He nuclear reaction. Results have been obtained on polycrystalline α-ZrO_2 ceramics and YSZ single crystals implanted with 3-MeV ^{3}He ions at a depth around 7 μm then isochronously annealed in air at temperatures between 200 and 1100 °C. In α-ZrO_2, no change of the depth profile is found up to 800 °C. In contrast, two regimes are found in YSZ: (i) below 800 °C, diffusion is controlled by helium trapping at native oxygen vacancies (≈10 at.%), (ii) above 800 °C, helium escapes out of the profile, with almost complete outgassing at 1100 °C.

PACS: 66.30; 61.72.S; 81.70.J; 24.30.−v

1. Introduction

Stabilized cubic zirconia (ZrO_2) is a refractory material (melting point, $T_m = 2780$ °C) that is widely used for various industrial applications and considered to be a potential inert matrix for actinide immobilization or transmutation [1]. Due to the α-decays, the helium content could reach large values (>1 at.%) for long-term ageing [2]. Since the solution energy of helium in solids is large ($\geqslant 3$ eV) [3], He atoms will tend to coalesce and form bubbles inducing detrimental modifications of the material structure and mechanical properties (e.g. embrittlement) [4]. First steps of these processes involve atomic diffusion at moderate or high temperatures depending on the nuclear application.

However, data on helium migration are scarce in this material [5], as well as in other inert oxide matrixes, in contrast to transition element metals which have been thoroughly investigated in this field [4]. Such data are nonetheless necessary to implement models on helium behavior (diffusion, coalescence, bubble nucleation and growth) that could eventually induce swelling and material damage. The study of the diffusion of implanted helium, in conditions similar to radiogenic helium production, is thus an important issue.

Since the standard ion-beam techniques (RBS or ERDA) cannot be used to analyze helium at large depths [6] corresponding to ion implantations in the MeV range, we have thus studied the thermally activated migration of ^{3}He atoms using the resonant ^{3}He(d, p)^{4}He nuclear reaction, where ^{3}He acts as a tracer of ^{4}He diffusion with an isotopic factor correction. Such a reaction was already used a long time ago to profile helium deeply implanted in Nb by detecting the protons emitted at about 13 MeV [7]. The slowing down of deuterons in

* Corresponding author.
E-mail address: jean-marc.costantini@cea.fr (J.-M. Costantini).

0022-3115/$ - see front matter © 2003 Elsevier B.V. All rights reserved.
doi:10.1016/S0022-3115(03)00280-0

the matrix allows a scanning of the ^{3}He depth profile with no contribution of the matrix. Studies of helium diffusion in Ni and Zr were performed later with a deuteron milli-beam by detecting the recoiling α particles at smaller implantation depths [8,9]. The depth profile was deduced from the α particle spectrum by a deconvolution procedure. Our aim was then to apply the same technique based on proton detection with deuteron micro-beams or milli-beams delivered by nuclear probe facilities. Although the depth resolution and sensitivity of this NRA technique are known to be low [6], we show that helium migration can nevertheless be monitored by ^{3}He depth profiling.

2. Experimental

We used zirconia sintered ceramics of 100% pure monoclinic structure (α-ZrO_2) and mass density around 95% of the theoretical density (5.8 g cm^{-3}). The bulky sintered ceramics were machined into discs of 10-mm diameter and 1-mm thickness, annealed at 800 °C in air, and polished for analysis. Micrographic examinations showed that grain sizes were smaller than 40 μm. We also used polished yttria-stabilized zirconia (YSZ) single crystal plates ($5\times10\times1$ mm^3) with 9.5 mol.% yttria content ($Zr_{0.8}Y_{0.2}O_{1.9}$) of cubic fluorite structure (5.93 g cm^{-3}) with the $\langle 1\,0\,0\rangle$ orientation provided by Crystal GmbH Company (Berlin, Germany). Implantations in the YSZ single crystals with 3-MeV ^{3}He ions were performed at the Laboratoire PHASE (CNRS, Strasbourg, France) with a 7° angle tilt off the $\langle 1\,0\,0\rangle$ axis at a fluence of 1.7×10^{16} cm^{-2} (±5%) (2.6×10^{20} cm^{-3}, i.e. around 0.30 at.% at the peak of the distribution). The zirconia ceramics were implanted at the same fluence at normal incidence. The mean projected range (R_p) in such 'random' conditions is 6.93 μm with a longitudinal range straggling (ΔR_p) of 327 nm, as computed with the TRIM96/SRIM2000 code [10]. The beam was swept over the samples surface in order to obtain homogeneous implantations.

Thermal annealing of different samples was then performed in air at 400 and 800 °C during 1 h for the monoclinic zirconia ceramics and at temperatures between 200 and 1100 °C for the YSZ single crystals during 1/2 or 1 h (Tables 1 and 2). In the case of α-ZrO_2 ceramics, no further annealing at temperature higher than 800 °C was performed due to the phase transition to the tetragonal β-ZrO_2 phase starting at around 1000 °C.

^{3}He depth profiling was then achieved with the resonant ^{3}He(d, p)^{4}He nuclear reaction [7–9] on as-implanted and thermally annealed samples. These measurements were first carried out at the nuclear microprobe facility of the Laboratoire Pierre-Süe (CEA/Saclay, France) by using a deuteron micro-beam at normal incidence with

Table 1
Optimized values of the integrated areas (A), centroids (x_c), and standard deviations (s) of the Gaussian ^{3}He depth profiles in 3-MeV ^{3}He ion-implanted zirconia samples annealed during time t_a at temperature T, and effective diffusion constants (D^*) deduced from the 13-MeV proton yield curves obtained with the deuteron micro-beam (Fig. 1(a) and (b))

Samples	T (°C)	t_a (h)	A (arb. u.)	x_c (μm)	s (μm)	D^* (cm^2 s^{-1})
As-implanted monoclinic ceramics			3.90	6.50	0.32	
As-implanted YSZ single crystal			3.76	6.43	0.28	
YSZ single crystal	200	1/2	3.09	6.09	0.28	
YSZ single crystal	330	1	3.76	5.65	1.05	1.5×10^{-12}
YSZ single crystal	580	1	4.08	5.88	1.52	3.1×10^{-12}
Monoclinic ceramics	800	1	3.76	6.50	0.34	
YSZ single crystal	1100	1	0.03	6.65	0.45	

Table 2
Optimized values of the integrated areas (A), centroids (x_c), and standard deviations (s) of the Gaussian ^{3}He depth profiles in 3-MeV ^{3}He ion-implanted YSZ single crystals annealed during time t_a at temperature T, deduced from the excitation curves obtained with the deuteron milli-beam (Fig. 2). The effective diffusion constants (D^*) are deduced by using the reference standard deviation ($s_0 = 0.327$ μm) given by the SRIM2000 simulation [10]

T (°C)	t_a (h)	A (arb. u.)	x_c (μm)	s (μm)	D^* (cm^2 s^{-1})
200	1/2	1.01	6.54	0.40	1.5×10^{-13}
330	1	0.90	6.01	1.50	3.0×10^{-12}
580	1	0.97	6.75	2.37	7.7×10^{-12}
800	1	0.68	7.32	2.37	7.7×10^{-12}
930	1	0.03	7.17	1.26	

focal spot sizes ranging between 40×40 and 80×80 μm^2, and beam currents between 3 and 8 nA. Complementary cross check measurements were also performed at the Van de Graaff accelerator of the INSTN (CEA/Saclay) with a deuteron milli-beam of around 0.5-mm spot size at normal incidence and beam currents between 37 and 50 nA. It gave a maximum beam current density of 500 μA cm^{-2} in the former case, and 25 μA cm^{-2} in the latter. No effect of the beam current density ranging from 20 to 400 μA cm^{-2} was found with the milli-beam.

For the micro-beam measurements, charged particle spectra were recorded with an annular surface barrier detector with a 1500-μm depletion length and energy resolution of 25 keV at a detection angle between 170° and 175°. A 25-μm thick mylar energy filter was used to stop the backscattered deuterons and the α particles from the ^{16}O(d, α) reaction, in order to decrease the detector's dead time. For the milli-beam measurements, the surface barrier detector was set at 150° with a 29-μm mylar screen. The broad proton peak appears at about 13 MeV in a low background region well separated from the low-energy protons due to the ^{16}O(d, p) and ^{12}C(d, p) reactions which were used for energy calibration.

We have plotted the curves of the 13-MeV proton yield [7], normalized by a deuteron integrated charge of 5 μC with the micro-beam and 40 μC with the milli-beam, versus the deuteron incident energy. The experimental excitation curve is the convolution integral of the ^{3}He depth profile with the reaction cross section and the energy spread of the incident ions. Since the cross section of this reaction shows a maximum for a deuteron energy near 430 keV with a FWHM around 350 keV [6,11], it gives here a maximum proton yield at around 1.3 MeV. The beam energy was progressively decreased from 2.0 to 0.7 MeV by variable steps from 100 to 25 keV near the curve maximum. Around 15 min acquisition time was necessary to record the spectra with sufficient statistics for each deuteron energy.

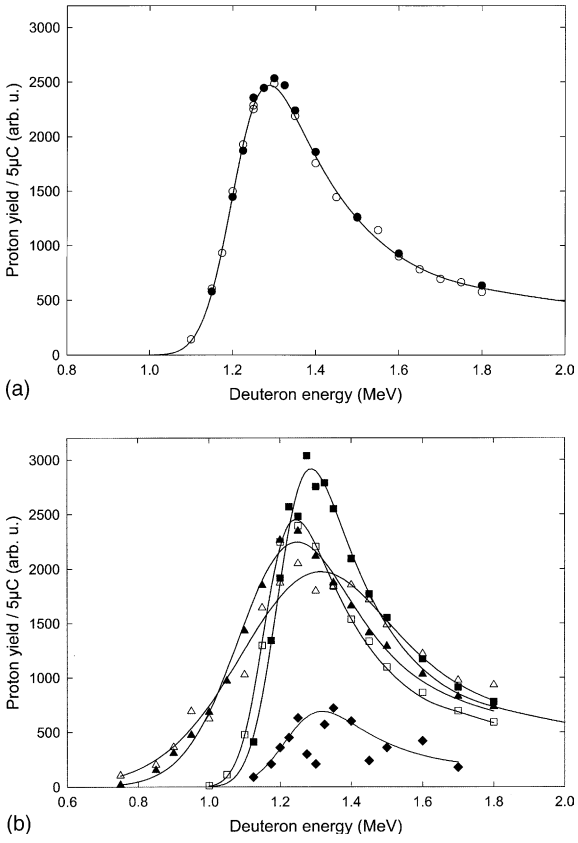

Fig. 1. (a) Yield of 13-MeV protons versus deuteron incident energy obtained with a micro-beam for polycrystalline monoclinic zirconia ceramics as-implanted with 3-MeV ^{3}He ions (open circles), and thermally annealed 1 h at 800 °C (full circles). The solid line is a least-squares fitted curve with the optimized parameters of the as-implanted Gaussian ^{3}He depth profile given in Table 1. (b) Yield of 13-MeV protons versus deuteron incident energy obtained with a micro-beam for YSZ single crystals as-implanted with 3-MeV ^{3}He ions (full squares), and thermally annealed 1/2 h at 200 °C (open squares), 1 h at 330 °C (full triangles), 1 h at 580 °C (open triangles), and 1 h at 1100 °C (full diamonds, magnification ×30). The solid lines are least-squares fitted curves with the optimized parameters of the Gaussian ^{3}He depth profiles given in Table 1.

3. Results

The excitation curves of ^{3}He in as-implanted and thermally annealed polycrystalline monoclinic zirconia and YSZ single crystals were obtained either with the deuteron micro-beam (Fig. 1(a) and (b)) or the milli-beam (Fig. 2). All data were fitted by a model where the proton yield $Y(E_0)$ at a given incident deuteron energy (E_0) is the convolution of the ^{3}He concentration depth profile $\rho(x)$ with the ^{3}He(d, p)^{4}He reaction cross section (σ) [12]. Since σ depends only weakly on the detection angle in the considered energy and angular range [11], we have thus neglected the angular dependence of the proton yield which writes [8]:

$$Y(E_0) = \int_0^{x_0} \sigma[E(x)]\rho(x)\,\mathrm{d}x, \tag{1}$$

where x_0 is the deuteron projected range, and $\sigma[E(x)]$ the total cross section for the deuteron energy $E(x)$ at depth x as given by the TRIM96/SRIM2000 computer code [10].

The helium concentration depth profile $\rho(x)$ was approximated by a Gaussian curve, as is frequently done in the case of an implantation profile where the 3rd-order ('skewness') and 4th-order moments ('kurtosis') of the distribution are neglected [13]:

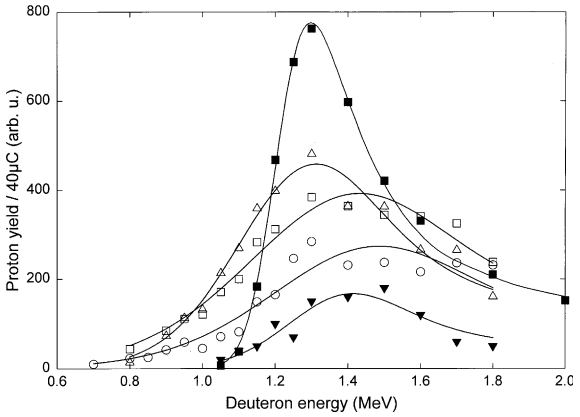

Fig. 2. Yield of 13-MeV protons versus deuteron incident energy obtained with a milli-beam for YSZ single crystals implanted with 3-MeV ^{3}He ions and thermally annealed 1/2 h at 200 °C (full squares), 1 h at 330 °C (open triangles), 580 °C (open squares), 800 °C (open circles), and 930 °C (full triangles, magnification × 10). The solid lines are least-squares fitted curves with the optimized parameters of the Gaussian ^{3}He depth profiles given in Table 2.

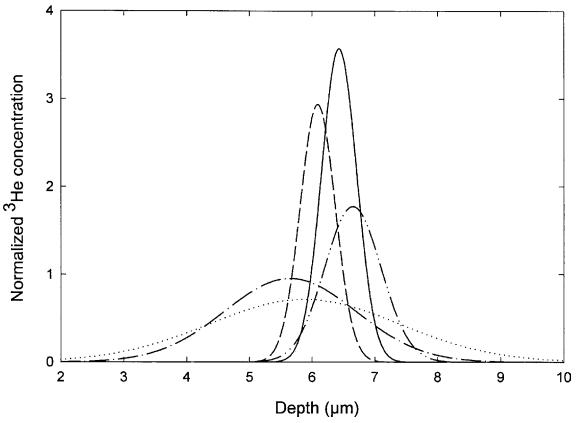

Fig. 3. ^{3}He Gaussian depth profiles normalized to the as-implanted integrated area (A_0) deduced from the 13-MeV proton yield curves obtained with a deuteron micro-beam for as-implanted (solid) and annealed YSZ single crystals: 200 °C (dash), 330 °C (dash-dot), 580 °C (dot), and 1100 °C (magnification × 100; dash-dot-dot).

$$\rho(x) = (A/s\sqrt{2\pi})\exp[-(x-x_c)^2/2s^2], \quad (2)$$

A is the depth profile integrated area proportional to the helium fluence, x_c the centroid of the distribution which for the as-implanted profile must be near the mean projected range of the ^{3}He ions (R_p), and s the standard deviation near the longitudinal range straggling (ΔR_p). The three parameters (A, x_c, s) were optimized by an IMSL modified Levenberg–Marquard algorithm which minimizes a normalized quadratic error function between the simulated and experimental curves (see the fitted curves in Figs. 1 and 2 with an error less than 5% per point and best fitted values of A, x_c, s in Tables 1 and 2). For this purpose, a specific computer program (AGEING) was developed in a PV-wave/GUI environment.

For the as-implanted polycrystalline monoclinic zirconia (α-ZrO_2) and YSZ single crystal, it is seen that the agreement is good between x_c and R_p (6% deviation) on the one hand, and s and ΔR_p (2% deviation) on the other hand (Table 1) like in a previous study on helium diffusion in britholite (fluorapatite) ceramics [12]. Depth profiles $\rho(x)/A_0$ normalized to the as-implanted integrated area (A_0) are shown in Fig. 3 for YSZ single crystals. We have previously shown [12] that the ^{3}He depth profiles obtained by this convolution procedure was in very good agreement with the results based on the SIMNRA computer code [14]. In α-ZrO_2, no effect on the proton yield curve (Fig. 1a) and depth profile parameters (Table 1) was seen up to 800 °C within experimental resolution. In contrast in the YSZ, s increased markedly up to a factor 7 at 800 °C and decreased above. The distribution was slightly displaced towards the surface below 580 °C then shifted back. In contrast, the remaining ^{3}He content proportional to A remained almost constant up to 580 °C, then decreased by a factor around 0.3 at 800 °C, 30 at 930 °C, and 100 at 1100 °C (Tables 1 and 2). Although the milli-beam data yielded broader depth profiles than the micro-beam ones, the same overall features were found when the annealing temperature was increased. Despite these systematic discrepancies, it is seen that micro and milli-beam data are in good agreement in the variations of s and A normalized to the as-implanted values (s/s_0 and A/A_0) versus annealing temperature (Fig. 4).

Hence, the helium effective diffusion constant (D^*) for this concentration at a given temperature was deduced according to the relation [15,16]:

$$D^* = (s^2 - s_0^2)/2t_a, \quad (3)$$

where t_a stands for the annealing time, s_0 for the standard deviation of the as-implanted profile and s the standard deviation after annealing (Tables 1 and 2). It is to be noted that an isotopic correction factor of $\sqrt{4/3}$ must be applied to our D^* values for ^{3}He in order to obtain the ^{4}He diffusion constants. The resolution limit on s values of 0.01 μm leads to a relative error on D^* ranging between 2% and 14%. The milli-beam data of YSZ give D^* values twice as large as the micro-beam data due to the above-mentioned discrepancies on s values. However, an almost athermal behavior is found for D^* in both sets of data.

4. Discussion

Three different mechanisms of helium diffusion in solids are known to occur: the interstitial, substitutional

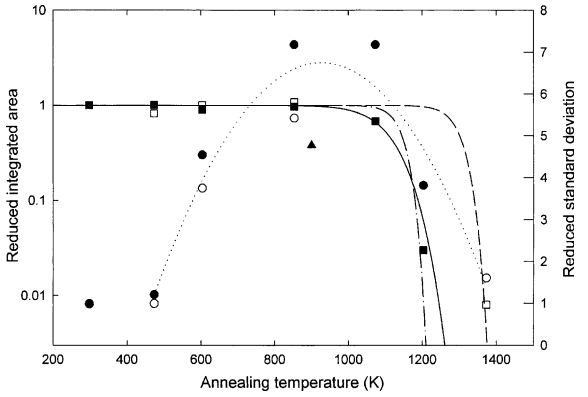

Fig. 4. ^{3}He Gaussian depth profile integrated area (A/A_0) (squares, left scale) and standard deviations (s/s_0) (circles, right scale) normalized to the as-implanted values deduced from the micro-beam (open symbols) and milli-beam (full symbols) data versus annealing temperatures for YSZ single crystals, with a least-squares fitted curve for A/A_0 (solid) and least-squares fitted parabolic one for s/s_0 (dot). Calculated isochronal annealing curves with $\Delta H = 4.0$ eV and $\nu = 10^{13}$ s^{-1} (dash-dot), and $\Delta H = 4.6$ eV and $\nu = 10^{13}$ s^{-1} (dash) are also displayed with a data point (full triangle) of helium release in YSZ ceramics [5].

and dissociative ones [3,4]. In metals, it is fairly well established that the interstitial mechanism operates only at low temperatures (<100 K) with small migration enthalpies (e.g. <0.5 eV in b.c.c. transition metals) [3]: as temperature rises helium atoms are rapidly trapped by the native or irradiation-induced vacancies since the solution energy is large ($\geqslant$ 3 eV) [3,4]. Helium diffusion at high temperatures or under displacive irradiation proceeds either through a substitutional mechanism involving the vacancy-assisted migration or through the dissociative mechanism involving helium-vacancy (V) clusters $(\mathrm{He_n}$–$V_\mathrm{m})$ in which helium atoms are trapped [8]. It is to be noted that the former process requires a large vacancy concentration in order to take place. In the latter process, the $(\mathrm{He_n}$–$V_\mathrm{m})$ clusters at large He concentrations can act as nucleation centers for gas bubbles [3,4].

The present results on zirconia clearly show that no effect on the ^{3}He depth profile is observed within experimental resolution in the polycrystalline ceramics with the monoclinic crystal structure after annealing up to 800 °C. In contrast, an increasing broadening of the depth profile is seen after isochronal annealing of the cubic YSZ single crystals up to 800 °C. At temperatures higher than 800 °C, the He content (A) decreases and s decreases back towards the as-implanted value (Fig. 4). Almost complete outgassing is achieved at 1100 °C.

In polycrystalline YSZ ceramics, for 200-keV and 1-MeV ^{4}He ion implantations in a low-fluence range $(1.4\times10^{13}$–1.4×10^{15} cm$^{-2})$, it was concluded that the activation energy (1.6 eV) found by thermal helium desorption spectroscopy (THDS) corresponds to vacancy-assisted diffusion [5]. At larger fluences $(1.4\times10^{16}$ cm$^{-2})$ a different mechanism occurs due to pressurized bubble formation [5]. In samples implanted with 200-keV ^{4}He ions at 700-nm depth, neutron depth profiling (NDP) data show that 'after annealing at 600 K the amount of helium and its spatial distribution in the sample are effectively unchanged for both high and low fluence' [5]. At low fluence $(1.4\times10^{15}$ cm$^{-2})$ all the helium was released after annealing at around 630 °C, whereas at high fluence $(1.4\times10^{16}$ cm$^{-2})$ a 62% helium release was found with a depth profile FWHM narrowing from 200 to 135 nm [5]. This small FWHM at 200 keV gives an helium peak concentration twice as large as in our case, i.e. 0.66 at.%, for around the same helium fluence. Helium bubble formation is thus favored at such a large concentration.

In the present case, at 0.3 at.%, it is striking to note that helium migration is indeed enhanced in the cubic YSZ single crystals with respect to the cubic YSZ [5] and monoclinic zirconia ceramics. However, a very weak dependence of the effective diffusion constant against annealing temperature is found below 800 °C. It looks like the diffusion process is dominated by trapping of implanted helium by vacancies as often found in the case of some metals [8,9,17,18]. Around 100 displaced atoms per incoming 3-MeV He ion are produced in the implantation process, along the damage profile, as computed with the SRIM2000 code [10] on the basis of a mean displacement energy threshold of 40 eV for both Zr and O atoms [19]. This yields an upper bound of the mean irradiation-induced vacancy concentration (V_Zr and V_O) near 10^{21} cm^{-3}, i.e. around 1 at.%, not taking account of the vacancy-interstitial recombinations.

In YSZ this is negligible compared to the large amount of native oxygen vacancies (V_O) at a concentration (C_V) near 10 at.% present in the bulk of the crystals. For thermal treatments performed under oxidizing atmosphere, no change of the oxide non-stoichiometry is expected in YSZ due to the charge compensation of Y^{3+} ions substituted for Zr^{4+} ions, with the electroneutrality condition $C_V \approx C_Y/2$ [20]. Such a large native defect density favors a substitutional or dissociative diffusion mechanism. The pressurized bubble mechanism as suggested by Damen et al. for polycrystalline YSZ ceramics at large He content [5] is thus questionable in our case, since a progressive broadening of the depth profile does occur between 330 and 800 °C.

We believe instead that two regimes of helium migration are found in the present work. In the implantation process prior to annealing, all He atoms are trapped by neighboring native oxygen vacancies, since $\rho \ll C_V$, near the implanted helium ion end-of-range, whereby (He–V) clusters are formed. In the first diffusion regime below 800 °C, we think that a vacancy-assisted substitutional diffusion mechanism first occurs

and the D^* values deduced from depth profile broadening include both processes of diffusion and trapping [15]. We will base our discussion on only one kind of traps (V_O) far from saturation with a constant density (C_V) versus depth. Assuming that the concentration ($C_{He–V}$) of filled traps (the helium-decorated oxygen vacancies) is much smaller than C_V leads to the following diffusion equation [15]:

$$\partial\rho(x,t)/\partial t = D(T)\partial^2\rho/\partial x^2 - k(T)C_V\rho(x,t) + k'(T)C_{He–V}, \quad (4)$$

where $k(T)$ and $k'(T)$ stand respectively for the kinetic constants of the 1st-order reactions of trapping in (He–V) clusters and detrapping, and $D(T)$ the diffusion constant at temperature T.

Assuming in addition a local equilibrium in steady state conditions, one gets a new diffusion equation for the total He concentration $\rho' = \rho + C_{He–V}$ such as:

$$\partial\rho'(x,t)/\partial t = D^*(T)\partial^2\rho'/\partial x^2 \quad (5)$$

with an apparent vacancy-dependent diffusion constant (D^*) [15]:

$$D^* = D/(1 + kC_V/k'). \quad (6)$$

Assuming Arrhenius laws for the thermal dependences of D, k and k' one has:

$$D^* \approx D_0^* \exp(-\Delta E^*/k_B T) \quad (7)$$

with a prefactor D_0^* and an effective activation energy ΔE^* which writes:

$$\Delta E^* \approx \Delta E_m + \Delta E_d - \Delta E_t, \quad (8)$$

where k_B is the Boltzmann's constant, and ΔE_m, ΔE_t and ΔE_d are respectively the activation energies of helium migration, trapping and detrapping. Such an equation can lead to an almost athermal behavior of D^* if $\Delta E_m \approx \Delta E_t - \Delta E_d$. An experimental value near 0.2 eV is found here for ΔE^*.

At temperatures higher than 800 °C, detrapping from the (He–V) clusters takes place and an apparent profile narrowing is observed in both sets of data, in agreement with the data of YSZ ceramics [5] (see the data point of [5] plotted in Fig. 4). In this 2nd diffusion regime, helium outgassing is thus controlled by the gradient of total helium concentration between the sample surface and the trapping zone near the helium ion end-of-range. One writes that helium release to the surface follows the decrease of the filled trap concentration ($C_{He–V}$) according to a 1st order kinetics [15] that leads to a decrease of the helium content in the distribution such as:

$$dA = -Av_0 \exp(-\Delta H/k_B T)\, dt, \quad (9)$$

where v_0 is a characteristic attempt frequency factor, and ΔH the activation enthalpy for helium release. Integration gives a classical dependence for isochronal annealing during the annealing time t_a at temperature T:

$$A/A_0 = \exp[-v_0 t_a \exp(-\Delta H/k_B T)]. \quad (10)$$

A least-squares fit of Eq. (10) (solid line) in Fig. 4 gives $\Delta H = 1.73$ eV and $v_0 = 5.8\times10^4$ s^{-1}. The latter unphysical value probably stems from the small number of data points. We have therefore plotted 2 calculated isochronal annealing curves (Fig. 4) which seem to represent fairly well the fan of data with $\Delta H = 4.0$ eV (dot-dashed), and $\Delta H = 4.6$ eV (dashed) by fixing $v_0 = 10^{13}$ s^{-1} near the Debye frequency. Although no theoretical values are available for zirconia, the latter ΔH values are consistent with the calculated activation energy (3.9 eV) for the dissociative diffusion mechanism of (He–V) clusters with one vacancy in MgO [21], and experimental values ranging between 4.0 and 4.7 eV deduced from THDS and NDP measurements [22].

The stronger trapping in the ceramics below 800 °C could be explained by the contribution of grain boundaries on which bubble nucleation and growth could occur. Whether small bubbles are formed in the latter case should be examined by high-resolution transmission electron microscopy. As a starting point, the present results show anyway that the resonant ^{3}He(d, p)^{4}He nuclear reaction allows one to monitor the diffusion of helium atoms deeply implanted in a zirconia matrix at concentrations above 0.1 at.%, despite the low resolution of this NRA technique.

5. Conclusions

In this preliminary work, we have studied the helium migration in zirconia by a non-destructive ^{3}He depth profiling using the resonant ^{3}He(d, p)^{4}He nuclear reaction. For this, 3-MeV ^{3}He ions were implanted at a depth around 7 μm and a peak concentration near 0.3 at.%. The emission yield of 13-MeV protons was measured versus the deuteron incident energy for as-implanted and thermally annealed samples. By fitting calculated proton yield curves to the experimental data, the parameters of the assumed Gaussian ^{3}He depth profile were deduced before and after isochronal annealing at various temperatures. No effect is seen in the monoclinic zirconia (α-ZrO_2) ceramics after annealing 1 h at 800 °C, whereas depth profile broadening occurs after 1-h annealing at 330 °C in YSZ single crystals. Effective diffusion constants were deduced from the profile standard deviations. Two regimes are found: in the first one, broadening of the ^{3}He depth profile occurs up to 800 °C with an almost constant helium content. The quasi-athermal behavior of the effective diffusion constants is attributed to the contribution of helium trapping at native oxygen vacancies. A second regime of

helium release occurs above 800 °C, with almost complete helium release from helium-vacancy clusters after annealing at 1100 °C with an activation energy around 4 eV.

Acknowledgements

The authors thank F. Couvreur (CEA/Saclay), S. Saudé and Dr R. Grynszpan (DGA/CTA/LOT, Arcueil) for their help during the measurements at the nuclear microprobe. Fruitful discussions with Dr D. Mathiot (PHASE laboratory, Strasbourg) are greatly acknowledged.

References

[1] W.L. Gong, W. Lutze, R.C. Ewing, J. Nucl. Mater. 277 (2000) 239.
[2] W.J. Weber, R.C. Ewing, C.R.A. Catlow, T. Diaz de la Rubia, L.W. Hobbs, C. Kinoshita, Hj. Matzke, A.T. Motta, M. Nastasi, E.K.H. Salje, E.R. Vance, S.J. Zinkle, J. Mater. Res. 13 (1998) 1434.
[3] D.J. Reed, Radiat. Eff. 31 (1977) 129.
[4] S.E. Donnelly, J.H. Evans (Eds.), Fundamentals of Inert Gases in Solids, Plenum, New York, 1991.
[5] P.M.G. Damen, Hj. Matzke, C. Ronchi, J.P. Hiernaut, T. Wiss, R. Frommknecht, A. Van Veen, F. Labohm, Nucl. Instrum. and Meth. B 191 (2001) 571.
[6] F. Paszti, Nucl. Instrum. and Meth. B 66 (1992) 83.
[7] P.P. Pronko, J.G. Pronko, Phys. Rev. B 9 (1974) 2870.
[8] M.B. Lewis, K. Farell, Nucl. Instrum. and Meth. B 16 (1986) 163.
[9] M.B. Lewis, N.H. Packan, G.F. Wells, R.A. Buhl, Nucl. Instrum. and Meth. 167 (1979) 233.
[10] J.P. Biersack, L.G. Haggmark, Nucl. Instrum. and Meth. 174 (1980) 257, Available at <http://www.srim.org>.
[11] O. Bersillon, CEA/Bruyères-le-Châtel, Olivier.bersillon@cea.fr, private communication, compilation of experimental cross-section data up to 1988.
[12] J.M. Costantini, P. Trocellier, J. Haussy, J.J. Grob, Nucl. Instrum. and Meth. B 195 (2002) 400.
[13] M. Nastasi, J.W. Mayer, J.K. Hirvonen (Eds.), Ion-Solid Interactions. Fundamentals and Applications, Cambridge University, New York, 1996.
[14] M. Mayer, SIMNRA user's guide, Technical Report IPP 9/113, Max-Planck Institute für Plasmaphysik, Garching, 1997. Available at <http://www.physics.isu.edu/sigmabase/programs/simnra44.html>.
[15] J. Philibert, Diffusion and Matter Transport in Solids, Ed de Physique, Paris, 1985.
[16] H. Ryssel, I. Ruge, Ion Implantation, Wiley, Chichester, 1986.
[17] J. Roth, S.T. Picraux, W. Eckstein, J. Bøttiger, R. Berisch, J. Nucl. Mater. 63 (1976) 120.
[18] F. Zielinski, J.M. Costantini, J. Haussy, F. Durbin, J. Nucl. Mater. 312 (2003) 141.
[19] K.E. Sickafus, Hj. Matzke, Th. Hartmann, K. Yasuda, J.A. Valdez, P. Chodak III, M. Nastasi, R.A. Verall, J. Nucl. Mater. 274 (1999) 66.
[20] K. Sasaki, J. Maier, Solid State Ionics 134 (2000) 303.
[21] G. Busker, M.A. Van Huis, R.W. Grimes, A. Van Veen, Nucl. Instrum. and Meth. B 171 (2000) 528.
[22] A.V. Fedorov, M.A. Van Huis, A. Van Veen, Nucl. Instrum. and Meth. B 191 (2002) 452.